Catenary Tether Shape Analysis for a UAV - USV Team

Kurt A. Talke[1,2], Mauricio de Oliveira[2], Thomas Bewley[2]

Abstract— The quasi-static catenary curve of a semi-slack tether between an essentially stationary unmanned air vehicle (UAV) and a small unmanned surface vehicle (USV) is investigated and characterized. An empirical analysis, performed over a discretized space of vertical and horizontal separations of the two vehicles, determines an optimum cable length & tension for maximizing system robustness during the vertical heave of the USV due to high seas. Operating at this optimum condition allows for equal displacements of the USV in the up and down directions, minimizing the possibility of both fouling (with the tether touching the water) and excessive downforce on the UAV (with the tether pulled taut) during dynamic heave events. Scaling the horizontal offset, tether length, and tension by the flying height collapses all empirical results into convenient curves depending only on a nondimensional relative position parameter ($\Delta x/\Delta y$), accurately fit by low order polynomials. This eliminates the need for a lookup table, and decreases computation time during implementation. The heave robustness analysis results in a recommended operating relative position of $\Delta x/\Delta y \approx .46$. Experimental results are presented and confirm the catenary analysis for the proposed tether.

I. INTRODUCTION

Lightweight, agile, low cost, unmanned air vehicles (UAV) provide numerous capabilities for a variety of missions, but are often limited to short flight times due to their reliance on batteries. Similar to the pumping of fuel up to a rotorcraft [1], recent investigations have attempted to fly UAVs on power umbilical tethers, with a power source on the ground or sea surface providing essentially unlimited power and flight time [2] [3]. Such a persistence of flight capability can greatly benefit both emergency response efforts (by providing a secure communication network node or video surveillance point in the sky [4]) as well as various military Intelligence, Surveillance, and Reconnaissance (ISR) missions.

Most published work in the field of tethered flight are restricted to the taut tether case. Taut tether flight can be used to avoid dealing with tether oscillations [1], improve flight stability [5]–[9] or enhance landing capability [10]–[12]. These systems employ either no tether management while the UAV maintains tension [13], or a clutch-based winch mechanism that continuously reels in any slack tether length. Station keeping, where the UAV remains stationary is difficult for systems where the UAV controls tension. Taut tether flight may also be undesirable since it introduces downward
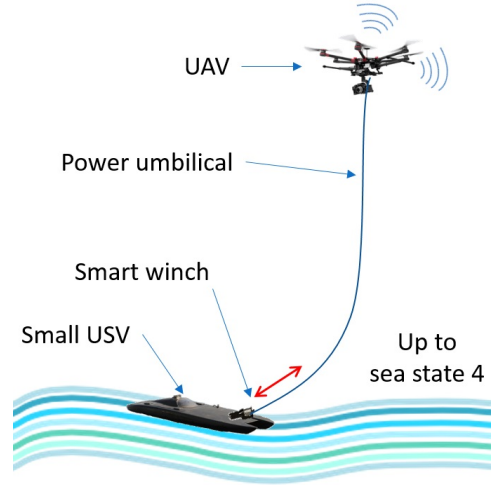
[1]Kurt Talke is with Space and Naval Warfare Systems Center Pacific, Unmanned Systems Advanced Development group, San Diego , CA 92110, USA kurt.talke@navy.mil

[2]Kurt Talke, Mauricio de Oliveira, and Thomas Bewley are with the Dept. of MAE, MC 041, UC San Diego La Jolla, CA 92093, USA mauricio@ucsd.edu, bewley@ucsd.edu

Fig. 1: Schematic of a tethered UAV USV team in up to sea state 4. The winch system controls tether length to account for the dynamic motion of the small USV, leaving the tether in a semi-slack, quasi-static state at all time.

forces on the UAV due to tether tension. These forces must be overcome by increasing UAV thrust, significantly reducing the UAV payload capacity and available power budget.

A few non-taut tether management systems have been previously proposed. A reactive tether management approach [14], where the tension and departure angle are measured at a winch, showed moderate winch controller results that can be further improved by incorporating knowledge of the UAV position. Another work used the measured tether length, tension, and depature angle as a means for non-GPS position estimation of the UAV based on a catenary cable model [4]. That work relied on a clutch-driven winch mechanism and on the UAV for tension control, with no consideration of total power budget. Neither of these examples consider the mission presented here, involving a highly dynamic moving base. Another non-taut tethered UAV approach worth mentioning uses a catenary cable model to determine the forces on the UAV for a flight controller [15]. Again, this work used a stationary base, and did not consider the problem of tether management.

The mission schematic for the tethered UAV system considered here is shown in Fig. 1. The UAV, flying at about 50 meters height, must maintain position and altitude for communication or ISR purposes. The UAV is tethered to a small Unmanned Surface Vehicle (USV) subject to a dynamic ocean environment. The tethered UAV configuration enables long duration missions (over 15 hours). Flying on a non-taut tether decreases power consumption and extends mission

duration. Management of the tether to reduce wasted energy while minimizing the risk of fouling are key considerations. A winch system is used to overcome disturbances and tether oscillations due to a dynamically moving base while the UAV remains essentially stationary.

This paper analyzes the static catenary hanging cable problem and develops a tractable tether management strategy driven by relative position and tether length. A recommended relative flying position is presented considering robustness to vertical motion of the USV. The key result is approximated using a low order polynomial, thus providing a computationally inexpensive approach for determining a reference tether length. The proposed model allows for a large range of flying positions while maximizing heave robustness with reduced overall power consumption. Experimental testing confirms the validity of the proposed catenary tether model.

The remainder of the paper is organized as follows. Section II derives the relevant catenary curve and heave robustness equations. Section III details the empirical analysis and nondimensionalization over the flying space. Section IV presents and discusses the empirical analysis results. Section V presents and discusses the experimental results. Section VI summarizes the key conclusions.

II. TETHER SHAPE ANALYSIS

The goal of the following analysis is to investigate the catenary cable equation based on the relative position of the endpoints, thus determining the cable length that can withstand the largest vertical motion of the base endpoint. The analysis assumes that the UAV can lift the cable weight and that a winch system operates fast enough to overcome dynamic heave disturbances, wind effects, and tether stiffness, i.e., the semi-slack tether is assumed to operate at near minimal tension in a quasi-static state. Thus, the static catenary equation may be applied, which considers only the cable weight and tension at endpoint locations. The ultimate goal of the project is to facilitate system operation in the presence of tether oscillations and wind loading associated with a Douglas sea state 4 [16] and Beaufort wind scale 4-5 [17], i.e., 1.25-$2.5m$ wave heights over a 5-15 second wave period and wind speeds of 11-21 knots.

A. Catenary Equation and Parameters Derivation

The free body diagram given in Fig. 2 is used to parameterize the catenary system. Point A, with angle α, is connected to the USV and the winch mechanism, while point B, with angle β, is connected to the UAV.

A balance of tangential tension and tether weight forces between points B and C, leads to the differential equation:

$$\tan(\beta) = \frac{dy}{dx} = \frac{\lambda g L}{T_0} \quad (1)$$

where L is the tether length, λ is the linear density of the tether, g is gravity, and T_0 is the horizontal tension at the vertex. The solution of (1) is given by the general form of the catenary equation [18]:

$$y = y_0 + a \cosh(\frac{x - x_0}{a}) = y_0 + \frac{a}{2}\left(e^{\frac{x-x_0}{a}} + e^{-\frac{x-x_0}{a}}\right) \quad (2)$$
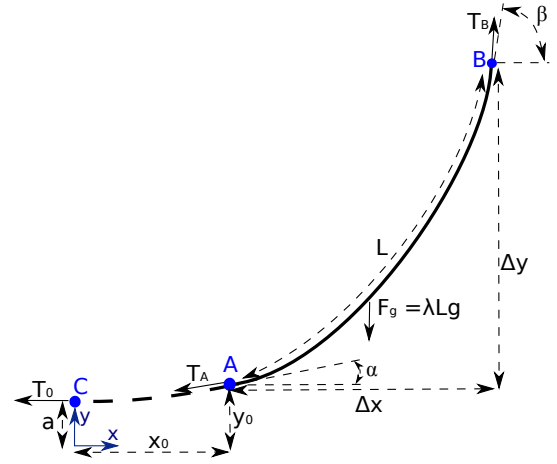

Fig. 2: Free body diagram of a catenary curve through specific endpoints. The weight of the tether, F_g, with length L, is offset by the tension at the endpoints, T_0 or T_A, and T_B. Δx and Δy correspond to the relative position, and drive the solution of catenary parameter, a. Point C, the vertex, is used for the determination of the resulting differential equation. x_0 and y_0 represent a shift in the coordinate system once the catenary parameter has been determined.

where y_0 and x_0 are the distances that shift the axes to point A, and a is the catenary parameter defined as:

$$a = \frac{T_0}{\lambda g} \quad (3)$$

In relation to the relative position of the endpoints A and B, the catenary parameter, a, can be found numerically from the transcendental equation [19]:

$$\sqrt{L^2 - \Delta y^2} = 2a \sinh(\frac{\Delta x}{2a}) \quad (4)$$

where $\Delta x, \Delta y$ are the relative positions and L is the known tether length.

The x-axis shift, x_0, can be found once the catenary parameter a has been determined by dividing the quantity $(L + \Delta y)$ and its corresponding catenary equation by $(L - \Delta y)$:

$$\frac{L + \Delta y}{L - \Delta y} = \frac{e^{\frac{x_B - x_0}{a}} - e^{\frac{x_A - x_0}{a}}}{-e^{-\frac{x_B - x_0}{a}} + e^{-\frac{x_A - x_0}{a}}} \quad (5)$$

where x_A and x_B are the x-coordinates of points A and B in the coordinate frame. Using the identity:

$$\frac{e^x - e^y}{e^{-y} - e^{-x}} = e^{x+y} \quad (6)$$

and solving for x_0 in (5):

$$x_0 = \frac{x_A + x_B}{2} - \frac{a}{2}\ln\left(\frac{L + \Delta y}{L - \Delta y}\right) \quad (7)$$

The y-axis shift, y_0, is found by substituting either endpoint into (2):

$$y_0 = y_A - a\cosh(\frac{x_A - x_0}{a}) = y_B - a\cosh(\frac{x_B - x_0}{a}) \quad (8)$$

where y_A and y_B are the y-coordinates of points A and B in this coordinate frame.

The departure angles, α and β, can be found by inserting the derivative of (2) with respect to x into (1).

$$\alpha = \arctan\left(\sinh\left(\frac{-x_0}{a}\right)\right), \ \beta = \arctan\left(\sinh\left(\frac{\Delta x - x_0}{a}\right)\right) \quad (9)$$

Performing a balance of forces for points A and B yields the tension at each point. Using the following identities:

$$\cos\left(\arctan\left(x\right)\right) = \frac{1}{\sqrt{1+x^2}}, \ \sin\left(\arctan\left(x\right)\right) = \frac{x}{\sqrt{1+x^2}},$$
$$\cosh^2(x) - \sinh^2(x) = 1 \quad (10)$$

and knowing that $\cosh(x) > 0$, one can find the tension without having to solve for the angles:

$$T_A = \frac{-\lambda g L \cos\beta}{\sin\alpha\cos\beta - \sin\beta\cos\alpha} = \frac{-\lambda g L \cosh\left(\frac{-x_0}{a}\right)}{\sinh\left(\frac{-x_0}{a}\right) - \sinh\left(\frac{\Delta x - x_0}{a}\right)} \quad (11)$$

$$T_B = \frac{-\lambda g L \cos\alpha}{\sin\alpha\cos\beta - \sin\beta\cos\alpha} = \frac{-\lambda g L \cosh\left(\frac{\Delta x - x_0}{a}\right)}{\sinh\left(\frac{-x_0}{a}\right) - \sinh\left(\frac{\Delta x - x_0}{a}\right)} \quad (12)$$

Given any relative position and tether length, all necessary parameters for the tether shape and tension are now known.

B. Heave Robustness

If the assumption that the winch can manage all dynamic disturbances fails, the effects on the UAV can be minimized by operating at a tether length, L_{rob}, best suited to handle heave, the vertical displacement of the USV. The heave robustness tether length allows for equal vertical displacement of the USV to specified limits while the tether length remains unchanged. As shown in Fig. 3, in the upward heave case, Δy_1, the limit is chosen to be the slack tether condition, where $\alpha = 0$. In the downward heave scenario, Δy_2, the limit is chosen to be a percentage increase in tension, T_{rob}, from the slack length tension, T_{slack}. For the upward heave scenario, where the vertex of the curve is at point A, i.e., $x_A = x_0 = 0$, we can substitute the derivative of (2) with respect to x, into (1), yielding:
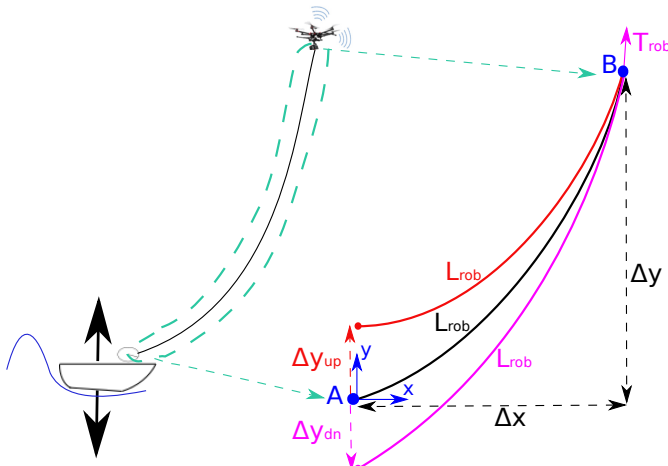
$$L = a_1 \ \sinh(\frac{\Delta x}{a_1}) \quad (13)$$

Fig. 3: Robustness margin determination for heave displacement of the lower endpoint. An operating tether length, L_{rob}, which gives equal heave tolerance both upward, Δy_1, and downward, Δy_2, is desired.

The new upward heave catenary parameter, a_1, can be found numerically for this transcendental equation, and Δy_1 can be solved as:

$$\Delta y_1 = \Delta y - a_1 \cosh\left(\frac{\Delta x}{a_1}\right) + a_1 \quad (14)$$

In the downward heave scenario, Δy_2 is introduced into (4), and the new catenary parameter, a_2, cannot be found numerically as both Δy_2 and a_2 are unknown:

$$L_{rob}^2 - (\Delta y_2 + \Delta y)^2 = 2a_2 \ \sinh(\frac{\Delta x}{2a_2}) \quad (15)$$

A so-called shooting method approach [20] can be used to find L_{rob}, by assuming $\Delta y_1 = \Delta y_2$. By first solving for Δy_1 using (14) for a given tether length, the catenary parameter, a_2, can be found using (15). With the tension found from (12), L_{rob} can then be found by iterating over the tether length, increasing the length from the slack length, L_{slack}, where $\alpha = 0$, until $T_B \geq T_{rob}$, at which point the tether length will be L_{rob}.

III. ANALYSIS OF FLYING SPACE

Due to the transcendental nature of (4), a purely analytic solution cannot be found. A "brute force" empirical analysis of the flying space can be performed to find an appropriate relative position for flying and robustness to heave tether length.

A. Analysis Limits

The flying heights of interest are in the range of $0 < \Delta y \leq 60m$. The corresponding horizontal offset is $0 < \Delta x \leq 60m$. Discretization is performed in $.5m$ increments. For each combination of relative positions, $(\Delta x_i, \Delta y_j)$, 480 tether lengths were considered, limited by a minimum length corresponding to the taut tether length and a maximum length chosen large enough to capture the minimum tension length. A sample discretization is shown in Fig. 4. Clearly, operational limits lie between the taut and slack tether length to ensure the tether does not sag into the water. The empirical analysis described involves solving for the minimum tension length, L_{Tmin}, departure angles, α, β, and tether tension, T_B, for each of the 480 tether lengths for all 14,400 combinations of relative position. A tether density of $\lambda = 0.042kg/m$ was used for analysis and experimentation.

B. Nondimensionalization

The empirical analysis for each flying height combination can be reduced by finding a scaling factor that results in a non-dimensional relative position parameter. By symmetry, the angles α and β for the taut, slack, and minimum tension tether shapes should be the same for any given value of $\Delta x / \Delta y$. By rearranging (4) and scaling the catenary parameter a by the relative height Δy, the nondimensional relative position parameter is indeed found to be $\Delta x / \Delta y$:

$$\sqrt{\left(\frac{L/\Delta y}{2a}\right)^2 - \left(\frac{1}{2a}\right)^2} = \sinh\left(\frac{\Delta x / \Delta y}{2a}\right) \quad (16)$$
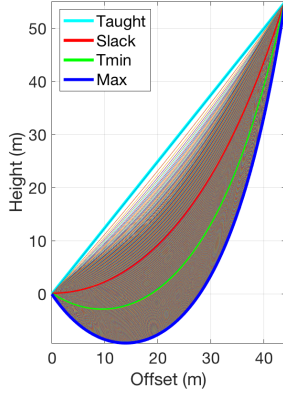
Fig. 4: Example catenary tether shape discretization for $\Delta y = 55m$ and $\Delta x = 44m$, with 480 tether lengths discretized evenly between $70.4m$ and $92.5m$. The taut tether is shown in cyan; slack tether, where $\alpha = 0$, in red; minimum tension tether in green; max length tether in blue.

The length is now also scaled by the relative height. The relative height scaling propagates through to the tension, as seen in (11) and (12), since tension scales linearly with length. Thus, the empirical analysis for each relative position can be combined by scaling the horizontal offset, tether length, and tension by the relative height at the endpoints.

IV. ANALYSIS RESULTS

The following results give a convenient model for determining the reference tension, length, and angle parameters for a given relative flying position.

A. Characteristic Result

The tether tension at the UAV for a flying height of $\Delta y = 55m$ and three horizontal offsets is shown in Fig. 5. These curves show that a minimum tension length exists, and that operating at that tether length minimizes the UAV thrust and power consumption. To the left of the minimum, tension increases rapidly due to the change in direction of the tension vector at the base. To the right of the minimum, the increase is much slower due to the fact that only tether weight increases while the tension vector direction remains relatively unchanged. In both Fig. 4 and Fig. 5, the minimum tension length is greater than the slack length and lies outside the operating region. The robustness to heave length lies in the critical region to the left of the slack length since the slack length is the maximum tether length limit due to the risk of fouling.

B. Heave Robustness Margins

The tolerance to vertical displacement of the USV results are shown in Fig. 6. The margins increase rapidly with offset until a maximum is reached around $25m$ in Fig. 6a, or at .46 in Fig. 6b for the 5% tension limit margin. The values taper off slowly thereafter. The inflection point corresponds to the point where the shooting method limiting factor switches from the slack length limit to the tension limit. It is also the recommended relative operating position,
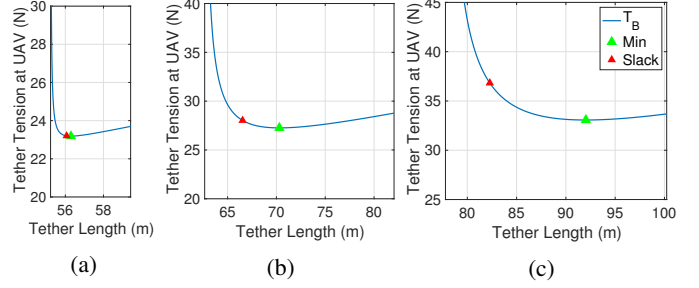

Fig. 5: Comparison of tether tension vs. length for $\Delta y = 55m$ and (a) $\Delta x = 5m$, (b) $\Delta x = 30m$, and (c) $\Delta x = 55m$. The slack length, shown by the red marker, is shorter and lies to the left of the minimum tension, shown by the green marker. The separation between these two points increases with offset (a)→(c).

where the difference between the upward and downward heave tolerance curves is largest.
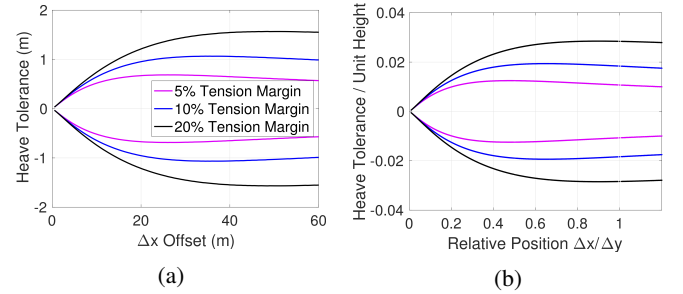

Fig. 6: Robustness margin empirical results as a function of offset (a) for $\Delta y = 55m$ and (b) combined nondimensionalized data. The two curves for each margin show the heave tolerance in both upward and downward directions, with the origin corresponding to no heave tolerance.

C. Tether Tension

Empirical results for the tether tension are shown in Fig. 7. For an offset less than 50% of the flying height ($\Delta x/\Delta y \leq .5$), the slack length and heave robustness length tensions remain nominally within 10% of the minimum tension. The nondimensionalized data shown in Fig. 7b combines all 14,400 empirical analysis "data" points into individual curves
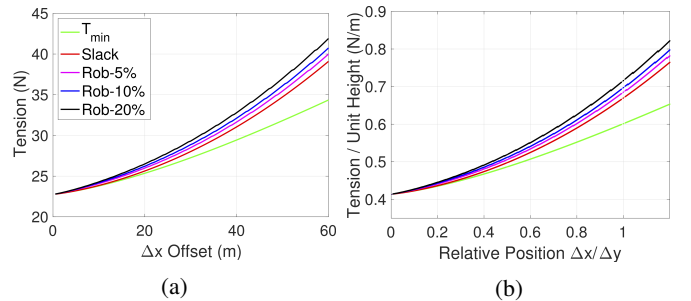

Fig. 7: Tension at the UAV empirical results as a function of offset (a) for $\Delta y = 55m$ and (b) combined nondimensionalized data. The heave robustness margin tether tensions have been plotted for a 5%, 10%, and 20% increase in tension from the slack length tension, and are shown slightly offset from the slack length tension curve.

TABLE I: Nondimensional tension polyfit coefficients

T	c_1	c_2	c_3	c_4	R^2
T_{min}	9.7864	2.0294	3.3904	-0.9513	1
T_{slack}	9.7886	2.0226	3.8953	0.1676	1
T_{rob5}	9.8038	2.5078	3.5501	0.3644	1
T_{rob10}	9.7940	2.8427	3.4364	0.4404	1
T_{rob20}	9.7838	3.1106	3.7257	0.3463	1

that can be approximated as a 3rd order polynomial:

$$T = \lambda \left(c_1 \Delta y + c_2 \Delta x + c_3 \frac{\Delta x^2}{\Delta y} + c_4 \frac{\Delta x^3}{\Delta y^2} \right) \quad (17)$$

with coefficients, c_1, c_2, c_3, c_4, and coefficient of determination, R^2, shown in Table I for normalized $\lambda = 1$. As seen in (12), the tether tension scales linearly with tether density. This is also true for the polynomial fit.

D. Tether Length

The tether length empirical results are shown in Fig. 8. The
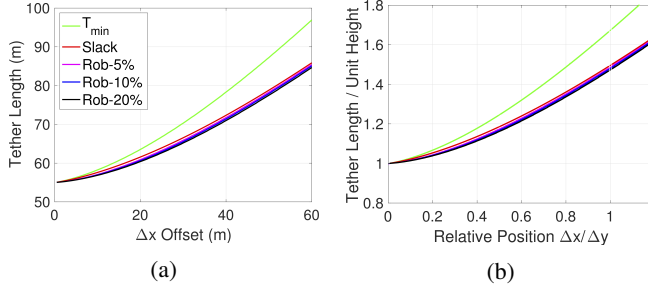
(a)   (b)

Fig. 8: Length empirical results as a function of offset (a) for $\Delta y = 55m$ and (b) combined nondimensionalized data. The tether length increases with offset as physically required, and again the heave robustness lengths offset the slack length data.

analysis data can again be fit into a 3rd order polynomial:

$$L = c_1 \Delta y + c_2 \Delta x + c_3 \frac{\Delta x^2}{\Delta y} + c_4 \frac{\Delta x^3}{\Delta y^2} \quad (18)$$

with the curve fit coefficients, c_1, c_2, c_3, and c_4, shown in Table II. Given the relative position, a reference length can be computed rather than using a lookup table. A quantitative test to determine the reference tether length using a computer with a 3.1Ghz processor and 16GB ram showed an increase in speed of 2300 times for the polynomial evaluation compared to using a lookup table. The least square curve fits have a $R^2 = 1$, giving high confidence in the fit. These polyfit coefficients are independent of linear density.

TABLE II: Nondimensional tether length polyfit coefficients

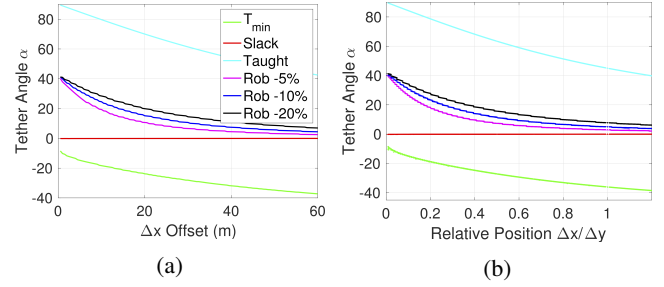| L	c_1	c_2	c_3	c_4	R^2
L_{min}	0.9972	0.2406	0.5849	-0.1497	1
L_{slack}	0.9976	0.2094	0.3752	-0.0862	1
L_{rob5}	0.9964	0.1514	0.4674	-0.1280	1
L_{rob10}	0.9974	0.1283	0.4888	-0.1335	1
L_{rob20}	0.9982	0.1127	0.4906	-0.12831	1

(a)   (b)

Fig. 9: Departure angle at boat empirical results as a function of offset (a) for $\Delta y = 55m$ and (b) combined nondimensionalized data. The minimum tension angle, shown in green, is negative, representing the tether dipping down into the water and a high risk of fouling. The heave robustness angles are shown within the operating region between the taut and slack length angles.

E. Departure Angles

The departure angle empirical results are shown in Fig. 9. For a horizontal offset less than 50% of the flying height, the heave robustness length angles vary between 40 and 10 degrees and track the minimum tension angle. Thereafter, they are bounded by the slack length angle. The nondimensional data is again modeled as a polynomial:

$$\alpha = c_1 + c_2 \frac{\Delta x}{\Delta y} + c_3 \left(\frac{\Delta x}{\Delta y} \right)^2 + c_4 \left(\frac{\Delta x}{\Delta y} \right)^3 + c_5 \left(\frac{\Delta x}{\Delta y} \right)^4$$

with curve fit coefficients, c_1, c_2, c_3, c_4, and c_5, shown in Table III. In order to keep the R^2 confidence value near 1, a 4th order and only a 2nd order fit were needed for the 5% heave robustness and taut angles, respectively. These polyfit coefficients are independent of linear density.

TABLE III: Nondimensional angle polyfit coefficients

α	c_1	c_2	c_3	c_4	c_5	R^2
α_{min}	-10.0482	-49.6974	36.8857	-13.2127	-	.99
α_{taut}	90.3299	-62.0733	16.7069	-	-	1
α_{rob5}	40.3217	-162.7497	309.9161	-280.6729	95.8555	.99
α_{rob10}	40.5363	-105.5804	116.5771	-46.5409	-	.99
α_{rob20}	41.6537	-84.6802	79.7592	-28.9605	-	.99

For the angle at the UAV, β, the difference in the minimum tension, heave robustness, and slack length angle is negligible. This is a benefit, since one does not need to reserve critical payload budget for a sensor to measure the angle.

F. Combined Results

By combining Fig. 6a, 7a, 8a, and 9a, for $\Delta y = 55m$, it can be argued that operating at a horizontal offset set point of $20m$ provides $\sim .75m$ heave tolerance in each direction. For this case, one sacrifices $<10\%$ increase in nominal tension, while having enough resolution in tether length and departure angle to control to the reference. While these figures exist for every combination of relative position in the analysis, the nondimenionalized curve fit polynomials give a single equation model for any flying position. Given the relative position, the reference heave robustness tether length can be determined, along with the predicted tether tension and

Fig. 11: Typical experimental results for tension vs. length, shown for $\Delta y = 18.29m$ and (a) $\Delta x = 6.10m$, and (b) $\Delta x = 12.19m$. The mean and standard deviation are shown on top of the empirical analysis results for 20 experiments at each cable length.
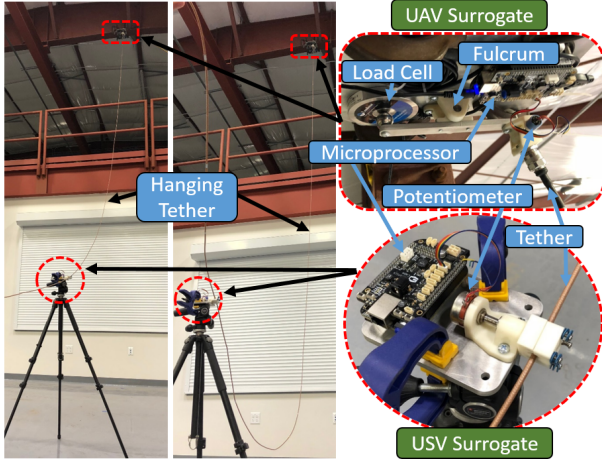

Fig. 10: Test setup showing two different length configurations on the left, and the UAV surrogate platform and USV surrogate platform on the right. Potentiometers collect departure angles, α and β, and a fulcrum converts the tension load into compression for a load cell to read. A microprocessor was used to read the data in both locations.

departure angles. Indeed, the recommended relative offset for maximizing heave robustness while keeping the nominal tension increase small is $\Delta x/\Delta y \approx .46$.

V. EXPERIMENTAL VALIDATION

The following experiment shows that the proposed tether for the given UAV/USV flight scenario conforms to the catenary analysis in Section IV-A and that the approximations detailed in the remainder of Section IV are valid.

A. Test Setup

The test setup to is shown in Fig. 10. The tether is rigidly mounted to a UAV surrogate platform capable of measuring the vertical component of the tether tension, T_{B_v}, and the departure angle, β. The tether is connected to a fulcrum that converts the tension load into compression for the load cell. At both the upper and lower ends of the tether, a potentiometer measures the departure angle. A microprocessor is used to record the data via a WiFi connection. Using the angle measurement and a force moment balance around the fulcrum, one can calculate the tether tension, T_B. The tether length was marked initially, and recorded for each measurement. Due to the limitations from the building height, testing was performed at three vertical offsets, $\Delta y = 4.87m$, $12.19m$, and $18.29m$. The horizontal offset for each started test at $\Delta x = 1.52m$, $3.05m$, and $3.05m$, respectively, and increased in increments of $1.52m$ until the vertical offset or the building limit max offset of $13.72m$ was reached.

B. Experimental Results

Static tether tension and departure angle experiments were performed for 18 combinations of vertical and horizontal offsets. Fig. 11 shows a typical result for the tension at the UAV surrogate, T_B. The experimental results agree with the empirical analysis for the two relative positions shown (the same agreement was observed for all other results). The
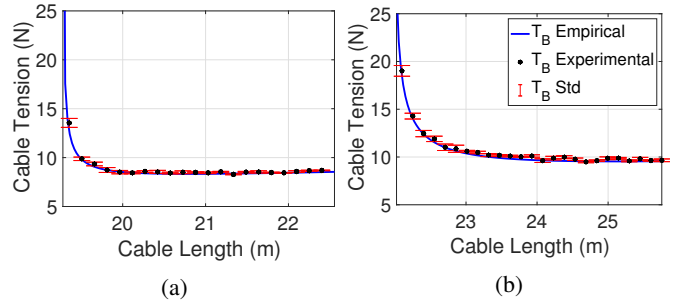
tension data capture the sharp decline, the minimum, and slow increase as the tether length increases. The small variability, shown by the standard deviation in the measurements is likely due to the tether not completely reaching steady state. Specifically, the standard deviation is greater at the shorter tether lengths. The tether exhibited small dynamic oscillations, particularly when under higher tension. The time for those oscillations to settle out was prohibitively long for data gathering purposes. Given enough time to settle, the standard deviation would likely decrease even more for the shorter lengths, higher tension measurements.

Table IV shows the mean error and standard deviation for all tension measurements of the 18 relative position experiments. All experiments had a mean error within 7% of the empirical catenary analysis. All but three of the experiments had a standard deviation of less than 3.6%. The three outliers were due to oscillations in the tether. The mean error and standard deviation for all measurements was $3.8\% \pm 3.3\%$. Comparing the three vertical offsets, we observe that the error decreases as Δy increases. Sensor measurement, setup, and cable density errors play a larger role at low Δy due to the smaller overall tensions.

TABLE IV: Tension experimental error $\pm$ standard deviation from empirical analysis per relative position

Δx	$\Delta y = 4.87m$	$\Delta y = 12.19m$	$\Delta y = 18.29m$
1.52m	6.4 % ± 2.9 %	-	-
3.05m	6.7 % ± 5.0 %	4.4 % ± 10.9 %	1.8 % ± 1.5 %
4.57m	2.7 % ± 2.0 %	4.0 % ± 3.4 %	4.5 % ± 5.6 %
6.10m	-	3.4 % ± 2.7 %	1.6 % ± 1.5 %
7.62m	-	3.2 % ± 2.3 %	4.9 % ± 2.9 %
9.14m	-	5.1 % ± 3.6 %	3.3 % ± 2.5 %
10.67m	-	3.0 % ± 2.1 %	3.5 % ± 2.0 %
12.19m	-	2.8 % ± 1.9 %	2.5 % ± 1.7 %
13.72m	-	-	2.7 % ± 2.8 %
Mean	5.2 % ± 3.3%	3.7 % ± 3.8 %	3.1 % ± 2.6%

Fig. 12 shows a typical result for the departure angle, α, at the base. The experimental departure angles agree with the empirical analysis results for the two relative positions shown. This is also observed for those results not shown. The measurements at each length did not vary significantly enough to justify a standard deviation calculation. Much of
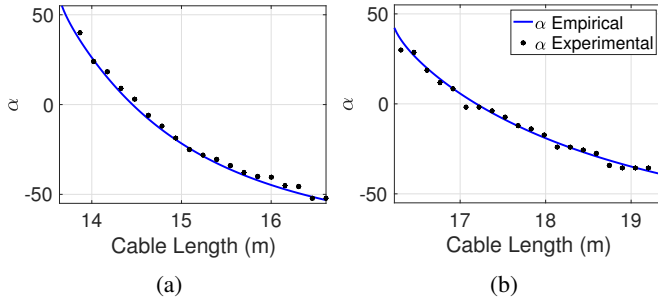
Fig. 12: Typical experimental results for α vs. length, shown for $\Delta y = 12.19m$ and (a) $\Delta x = 6.10m$, and (b) $\Delta x = 10.67m$. The experimental data shown is the mean of 20 measurements for each length.

the error between the empirical analysis and the experimental results can be attributed to the experimental setup. As seen in Fig. 10, the tether did not terminate at the base surrogate. The departure angle measurement clamped onto the tether, with the remaining tether maintaining the shape and departure angle only by being held properly by the data gatherer. Fortunately, this measurement, and associated error has minimal or no effect on the tension measurement, T_B, and the tension at the base, T_A, was not measured.

Fig. 13 shows typical results for the departure angle, β, at the UAV surrogate. The experimental departure angle results agree with the empirical analysis results for the two relative positions shown, as well as for those not shown. Again, the data did not justify a standard deviation calculation.
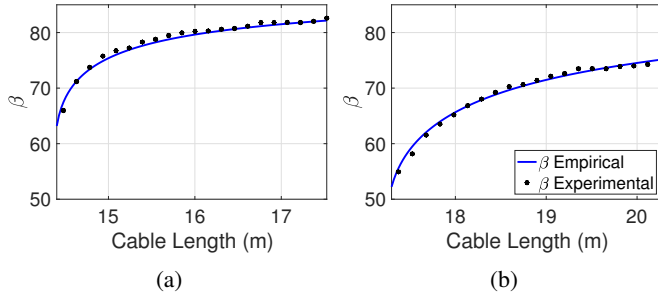

Fig. 13: Typical experimental results for β vs. length, shown for $\Delta y = 12.19m$ and (a) $\Delta x = 7.62m$, and (b) $\Delta x = 12.19m$. Each data point shown is the mean of 20 measurements.

Experimental results for these 18 operating conditions confirm the use of the catenary analysis approach for this specific hanging tether, and the analysis in Section IV.

VI. CONCLUSION

A quasi-static model using the catenary hanging cable equation was developed based on the relative position for a tethered UAV - USV team. An empirical analysis over the flying space determined a minimum tension and maximum heave robustness length for every flying condition. Division of the relative catenary parameters by the flying height transforms the analysis into nondimensional curves that can be approximated with low-order polynomials. The recommended relative offset for maximizing heave robustness is

$\Delta x/\Delta y \approx .46$. Experimental tension and departure angle results from 18 relative positions experiments confirmed that the catenary approach is valid. Follow-on work (already in progress) includes the development of a mechanized reel system, the development of a dynamic model, and a controller using this analysis as reference set point.

REFERENCES

[1] G. Schmidt and R. Swik, "Automatic hover control of an unmanned tethered rotorplatform," *Automatica*, vol. 10, pp. 393–394, Jan. 1974.

[2] C. Papachristos and A. Tzes, "The power-tethered uav-ugv team: A collaborative strategy for navigation in partially-mapped environments," in *22nd Mediterranean Conference on Control and Automation*, pp. 1153–1158, June 2014.

[3] S. Y. Choi, B. H. Choi, S. Y. Jeong, B. W. Gu, S. J. Yoo, and C. T. Rim, "Tethered aerial robots using contactless power systems for extended mission time and range," in *2014 IEEE Energy Conversion Congress and Exposition (ECCE)*, pp. 912–916, Sept 2014.

[4] S. Kiribayashi, K. Yakushigawa, and K. Nagatani, "Position estimation of tethered micro unmanned aerial vehicle by observing the slack tether," in *2017 IEEE International Symposium on Safety, Security and Rescue Robotics (SSRR)*, pp. 159–165, Oct 2017.

[5] L. A. Sandino, M. Bejar, K. Kondak, and A. Ollero, "On the use of tethered configurations for augmenting hovering stability in small-size autonomous helicopters," *Journal of Intelligent & Robotic Systems*, vol. 70, no. 1, pp. 509–525, 2013.

[6] M. M. Nicotra, R. Naldi, and E. Garone, "Taut cable control of a tethered UAV," *IFAC Proceedings Volumes*, vol. 47, no. 3, pp. 3190 – 3195, 2014. 19th IFAC World Congress.

[7] Y. Ouchi, K. Kinoshita, K. Watanabe, and I. Nagai, "Control of position and attitude of the tethered x4-flyer," in *2014 IEEE/SICE International Symposium on System Integration*, pp. 706–711, Dec 2014.

[8] S. Lupashin and R. D'Andrea, "Stabilization of a flying vehicle on a taut tether using inertial sensing," in *2013 IEEE/RSJ International Conference on Intelligent Robots and Systems*, pp. 2432–2438, Nov 2013.

[9] D. Ferreira de Castro, J. S. Santos, M. Batista, D. Antônio dos Santos, and L. C. Góes, "Modeling and control of tethered unmanned multicopters in hovering flight," in *AIAA Modeling and Simulation Technologies Conference*, American Institute of Aeronautics and Astronautics, June 2015.

[10] S.-R. Oh, K. Pathak, S. K. Agrawal, H. R. Pota, and M. Garratt, "Approaches for a tether-guided landing of an autonomous helicopter," *IEEE Transactions on Robotics*, vol. 22, pp. 536–544, June 2006.

[11] L. A. Sandino, D. Santamaria, M. Bejar, A. Viguria, K. Kondak, and A. Ollero, "Tether-guided landing of unmanned helicopters without gps sensors," in *2014 IEEE International Conference on Robotics and Automation (ICRA)*, pp. 3096–3101, May 2014.

[12] B. Ahmed and H. R. Pota, "Backstepping-based landing control of a ruav using tether incorporating flapping correction dynamics," in *2008 American Control Conference*, pp. 2728–2733, June 2008.

[13] M. M. Nicotra, R. Naldi, and E. Garone, "Nonlinear control of a tethered UAV: the taut cable case," *CoRR*, 2016.

[14] L. Zikou, C. Papachristos, and A. Tzes, "The power-over-tether system for powering small uavs: Tethering-line tension control synthesis," in *2015 23rd Mediterranean Conference on Control and Automation (MED)*, pp. 681–687, June 2015.

[15] B. Galea and P. G. Kry, "Tethered flight control of a small quadrotor robot for stippling," in *2017 IEEE/RSJ International Conference on Intelligent Robots and Systems (IROS)*, pp. 1713–1718, Sept 2017.

[16] "World of Earth Science: Douglas Sea Scale," Retrieved 9/9/2017. http://www.encyclopedia.com/science/encyclopedias-almanacs-transcripts-and-maps/douglas-sea-scale/.

[17] "Encyclopedia Britannica: Beafort Scale," Retrieved 9/9/2017. https://www.britannica.com/science/Beaufort-scale/.

[18] E. Lockwood, "Chapter XIII: The tractrix and catenary," in *A Book of Curves*, pp. 119–124, Cambridge, 1961.

[19] I. Todhunter, "XI flexible strings. inextensible, XII flexible strings. extensible," in *A Treatise on Analytical Statics*, pp. 238–285, Macmillan, 1958.

[20] T. Bewley, *Numerical Renaissance*. Renaissance Press, 2017.